ARTICLE

Near-Unity Electrochemical Conversion of Nitrate to Ammonia on Crystalline Nickel Porphyrin-based Covalent Organic Frameworks

Received 00th January 20xx,
Accepted 00th January 20xx

DOI: 10.1039/x0xx00000x

Fang Lv,†[a,b] Mingzi Sun,†[c] Yongpan Hu,†[a,b] Jie Xu,[a,b] Wei Huang,[a,b] Na Han,*[a,b] Bolong Huang *[c] and Yanguang Li *[a,b,d]

Electrochemical nitrate reduction can potentially enable the indirect fixation of atmospheric N_2, as well as the efficient nitrate removal from industrial wastewater, which has attracted rapidly increasing attention over recent years. It is, however, limited by the lack of efficient and low-cost electrocatalysts available so far. To address this challenge, we here demonstrate a two-dimensional nickel porphyrin-based covalent organic framework (COF) as a potential candidate for the first time. The product has a highly ordered molecular structure with abundant square-shaped nanopores. In neutral solution, the reduction of nitrate ions at different concentrations to ammonia is realized with great selectivity of ~90% under mild overpotentials, remarkable production rates up to 2.5 mg h^{-1} cm^{-2}, turnover frequency up to 3.5 s^{-1}, and intrinsic stability that is best delivered under pulse electrolysis. This cathodic reaction can also be coupled with the oxygen evolution reaction to permit full-cell electrolysis at high efficiency. Theoretical computations indicate that nickel centers can stably adsorb nitrate, and facilitate its subsequent reduction by lowering the energy barrier of the rate-determining step.

Broader context

Electrochemical nitrate reduction (NO_3RR) selectively to ammonia may play two essential roles within the artificial nitrogen cycle. When powered by renewable electricity, it can enable the indirect fixation of atmospheric N_2 without emission; it can also remove nitrates from industrial wastewater, and provide a needed remedy to the global environmental and water security challenge that we face today. Unfortunately, NO_3RR involves multistep electron transfers and can yield a spectrum of reduction products, giving rise to limited reaction selectivity. Copper so far represents the most studied catalyst, but generally requires large overpotentials in order to attain satisfactory NH_3 selectivity and production rates. Here, we demonstrate transition metal macrocycles as a potential candidate. As a proof of concept, we incorporate nickel porphyrin into two-dimensional covalent organic frameworks in order to maximize catalytic activity and efficiency. In the neutral solution, our catalyst exhibits great selectivity close to unity, excellent turnover frequency, and intrinsic stability. This work offers significant insights to extend promising electrocatalysts for nitrate reduction.

Introduction

Nitrogen is an indispensable ingredient for all living organisms. It exists in many different forms in the atmosphere, water, soils, and biota, which naturally interconvert via the nitrogen cycle.[1, 2] The development of the Haber–Bosch process more than a century permits the artificial conversion of atmospheric N_2 to NH_3, and since then has made ammonia fertilizers widely available.[3] Unfortunately, this industrial process is heavily energy intensive and has a massive carbon footprint. Direct NH_3 synthesis from electrochemical N_2 reduction under mild conditions is highly appealing, but is of formidable challenge and suffers from poor reaction rates (on the order of ~1 nmol s^{-1}) owing to the chemical inertness of N_2.[4-7] By comparison, NH_3 synthesis from nitrate/nitrite reduction reaction (NO_3RR or NO_2RR) is more kinetically favorable, and has attracted rapidly growing attention recently.[8-10] The nitrate or nitrite feed sources can be derived from N_2 via plasma treatments, thereby enabling the indirect fixation of atmospheric N_2;[11, 12] the reaction can be powered by renewable electricity from solar and wind, and is potentially emission-free. Moreover, NO_3RR or NO_2RR offers a viable solution to remove nitrates and nitrites in eutrophic water bodies from over-fertilization or other anthropogenic activities and may mitigate the global water security challenge that we face today.[13-15] However, NO_3RR or NO_2RR to NH_3 involves multistep electron transfers that generally compromise the reaction selectivity.[16] There have been increasing calls for the development of efficient NO_3RR or NO_2RR electrocatalysts at low costs.

---

[a] Institute of Functional Nano & Soft Materials (FUNSOM), Soochow University, Suzhou, 215123 China.
[b] Jiangsu Key Laboratory for Advanced Negative Carbon Technologies, Soochow University, Suzhou 215123, China.
[c] Department of Applied Biology and Chemical Technology, The Hong Kong Polytechnic University, Hung Hom, Kowloon, Hong Kong SAR, China.
[d] Macao Institute of Materials Science and Engineering (MIMSE), MUST-SUDA Joint Research Center for Advanced Functional Materials, Macau University of Science and Technology, Taipa 999078, Macau SAR, China.

† These three authors contribute equally.

*E-mail: yanguang@suda.edu.cn; bhuang@polyu.edu.hk; hanna@suda.edu.cn

Electronic Supplementary Information (ESI) available. See DOI: 10.1039/x0xx00000x

The following publication Lv, F., Sun, M., Hu, Y., Xu, J., Huang, W., Han, N., Huang, B., & Li, Y. (2023). Near-unity electrochemical conversion of nitrate to ammonia on crystalline nickel porphyrin-based covalent organic frameworks [10.1039/D2EE02647C]. Energy & Environmental Science, 16(1), 201-209 is available at https://dx.doi.org/10.1039/d2ee02647c.

Among different candidates, Cu-based catalysts have received the most attention and have been investigated in a number of recent studies.[17-19] They, however, generally demand large overpotentials in order to attain satisfactory NH_3 selectivity and production rates.[9, 20] On the other hand, transition metal macrocycles with discrete metal (in particular Fe, Co, and Ni) centers have found applications for a range of important electrochemical processes (*e.g.* oxygen reduction reaction and CO_2 reduction reaction),[21-24] but have never been considered for NO_3RR or NO_2RR to our best knowledge. Their diverse and well-defined molecular structures offer a unique opportunity to be used as the model catalyst and to understand the structure-activity correlation. It is also suggested that the isolated metal centers may suppress the undesirable N-N coupling and inhibit the side reaction pathway.[25] Unfortunately, transition metal macrocycles are often subjected to strong intermolecular π-π stacking, and form microsized crystals with low surface areas, which adversely impair their attainable activities.[26] Incorporating transition metal macrocycles within two-dimensional (2D) conjugated covalent organic frameworks (COFs) provides a promising strategy to address the above issue. The porous structure of COFs could significantly enhance the surface accessibility of active sites, and their molecular conjugation may also facilitate the rapid intralayer and interlayer electron transfer to the active sites during electrochemical reactions.

To this end, we here report a 2D nickel porphyrin-based COF (NiPr-TPA-COF) for efficient electrochemical NO_3RR to NH_3 in a neutral media. NiPr-TPA-COF features highly crystalline frameworks and has abundant mesoporosity. It exhibits great electrocatalytic activity and NH_3 selectivity of ~90%. A remarkable NH_3 production rate of up to 2.5 mg h^{-1} cm^{-2} and turnover frequency (TOF) of 3.5 s^{-1} are measured. Density functional theory (DFT) calculations suggest that the NiPr moieties can stably adsorb NO_3^-, and enable efficient electron transfer for its further reduction with a decreased energy barrier.

Results and discussion

NiPr-TPA-COF was synthesized from the Schiff base condensation reaction between 5,10,15,20-tetrakis(4-aminophenyl) porphinato nickel and terephthalaldehyde (TPA) in the presence of 6 M acetic acid as the catalyst (see ESI† for details). The slow and reversible crosslinking of amine and aldehyde precursors catalyzed by acetic acid triggers a self-correction mechanism that is proven essential to high product crystallinity.[27-29] In addition, we also prepared metal-free H_2Pr-TPA-COF as a control by replacing the NiPr precursor with H_2Pr under otherwise identical conditions.

Fig. 1a schematically depicts the structural topology of NiPr-TPA-COF consisting of the A-A stacking of 2D molecular layers with square shaped porosity, which is confirmed by its powder X-ray diffraction (XRD) pattern. The sharp diffraction peaks indicate long-range structural ordering and high product crystallinity (Fig. 1b). The most intense peak located at 3.45° is assignable to the (100) diffraction and corresponds to an average pore width of 2.5 nm in good agreement with the proposed structure. The molecular structure of NiPr-TPA-COF was further interrogated by a multitude of spectroscopic analyses. Compared to the two starting monomers, both the C=O stretching vibration (1697 cm^{-1}) and the N-H stretching vibration (3300-3500 cm^{-1}) disappear in the Fourier-transform infrared spectroscopy (FT-IR) spectrum of NiPr-TPA-COF. A new peak at 1617 cm^{-1} is instead observed in line with previous results,[30, 31] attesting to the complete condensation and the formation of the imine linkage (Fig. 1c). Raman analysis corroborates the formation of imine linkage by its characteristic signal at 1587 cm^{-1} (Fig. S1, ESI†).[32] Moreover, the imine functionalities are also reflected from the ^{13}C solid-state nuclear magnetic resonance (NMR) spectrum of NiPr-TPA-COF showing the resonance peak at δ = 158.6 ppm along with other signals from the porphyrin (Fig. S2, ESI†).[33] The X-ray photoelectron spectroscopy (XPS) of NiPr-TPA-COF supports the presence of Ni centers in the divalent state (Fig. S3, ESI†).[34] Spectroscopic characterizations of H_2Pr-TPA-COF reveal a similar molecular structure except for transition metal centers as summarized in Fig. S4 (ESI†).

NiPr-TPA-COF was subsequently subjected to microscopic imaging. Under low-resolution transmission electron microscopy (TEM), the product is unveiled to consist of square nanoflakes that are further stacked together (Fig. 1d). Individual nanoflakes have a lateral size of ~100 nm, and exhibit smooth edges and sharp corners. The square shape reflects the inherent four-fold symmetry of the molecular structure. Under high-resolution TEM, evident square fringes are observed with a d-spacing of 2.5 nm. These nanoflakes are determined to be terminated with (001) planes. Periodic mesoporous channels perpendicularly run through nanoflakes and correspond to the light contrast regions in Fig. 1e. The energy dispersive spectroscopy (EDS) elemental mapping in Fig. 1f shows the uniform spatial distribution of C, N, and Ni species and hence the composition homogeneity. The porous nature of NiPr-TPA-COF is additionally confirmed by BET analysis, which measures large surface areas of 899 m^2 g^{-1} and pore volume of 0.49 cm^3 g^{-1} (Fig. S5, ESI†). Combined together, the above results unambiguously support that the highly crystalline 2D COF is formed via the imide linkage and with the successful incorporation of NiPr moieties. Its ordered and porous structure facilitates fast mass transport and charge transport, which are highly needed for efficient electrocatalysis.

We next evaluated the electrochemical performance of NiPr-TPA-COF for NO_3RR in a two-compartment H-cell (see ESI† for details). The catalyst powder was dropcast onto a 1×1 cm^2 carbon fiber paper electrode at the mass loading of 1 mg cm^{-2}. Two control samples *i.e.* metal-free H_2Pr-TPA-COF and the NiPr monomer were brought into the comparison side by side. We initially attempted to run NO_3RR in 1 M KOH like many other studies did.[17, 35, 36] NiPr-TPA-COF delivered large current density and NH_3 selectivity superior to most competitors under similar conditions (Fig. S6, ESI†).[17, 36, 37] However, we surprisingly discovered that the current collector itself was electrochemically active in the alkaline medium (which would be the subject of our future study) and strongly interfered with our measurements (Fig. S7, ESI†). Therefore, all the experiments were carried out in the neutral solution where the activity of the bank current collector is minimized (Fig. S8, ESI†).

Fig. S9 (ESI†) depicts the polarization curves of NiPr-TPA-COF in Ar-saturated 0.5 M K_2SO_4 with and without 0.1 M KNO_3. In the absence of KNO_3, only the hydrogen evolution reaction (HER) takes

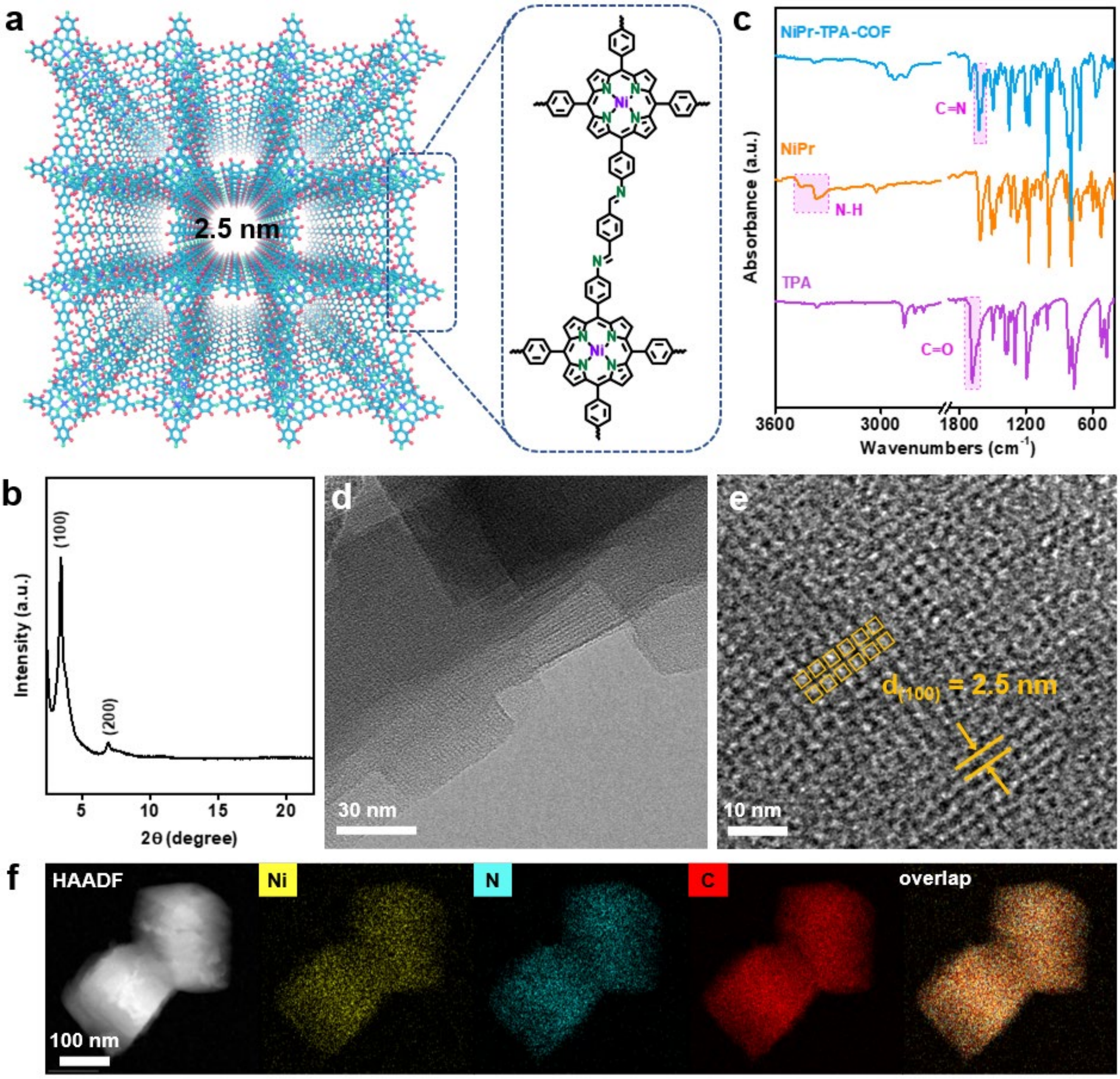

Fig. 1 Structural characterizations of NiPr-TPA-COF. (a) Schematic topology of NiPr-TPA-COF and its constituent units. (b) XRD pattern of NiPr-TPA-COF. (c) FT-IR spectra of NiPr-TPA-COF, NiPr, and TPA. (d) TEM image, (e) HR-TEM image, and (f) EDS elemental mapping of NiPr-TPA-COF.

place, and it doesn't exhibit appreciable current density till <-1.5 V (versus saturated calomel electrode or SCE, the same hereinafter). The addition of KNO_3 positively displaces the polarization curve. The current density starts to take off at -0.8 V and increases to 46 mA cm^{-2} at -1.5 V, which is the first indication of the great NO_3RR activity of NiPr-TPA-COF. By contrast, both H_2Pr-TPA-COF and NiPr have negligible cathodic responses in the presence of KNO_3 within the same potential region.

In order to identify and quantify the reduction products, chronoamperometric (i~t) analysis was conducted at different working potentials. The amount of NH_3 production was measured via the indophenol blue method using ultraviolet-visible (UV-Vis)

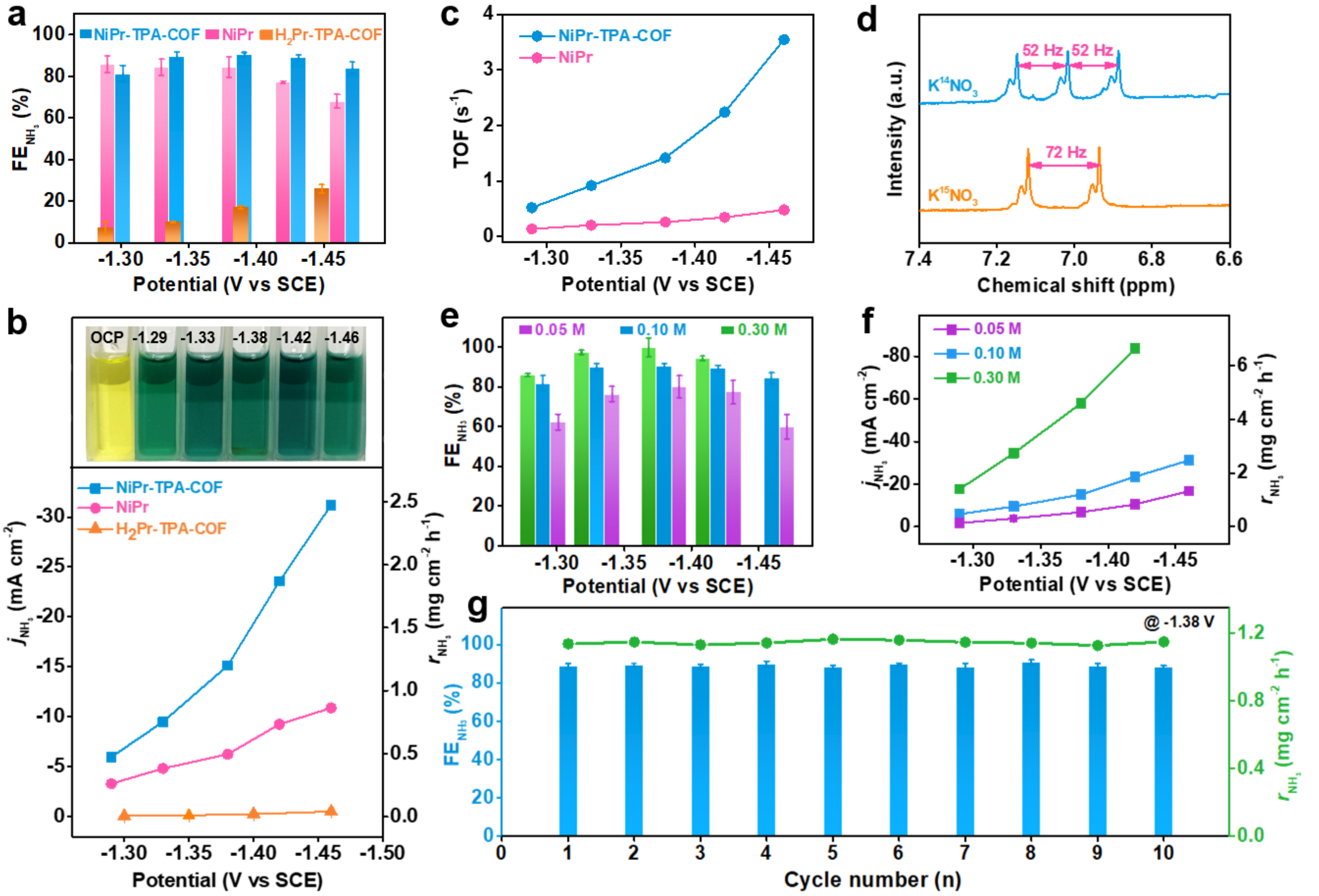

Fig. 2 Electrochemical NO_3RR performance of NiPr-TPA-COF. (a) NH_3 Faradaic efficiency and (b) NH_3 partial current density and production rate of NiPr-TPA-COF in comparison with those of H_2Pr-TPA-COF and NiPr; the top illustration in (b) shows the diluted catholyte after NO_3RR at different potentials and with the addition of the indophenol indicator. (c) TOF values of NiPr-TPA-COF and NiPr. (d) ^1H NMR spectra of NH_3 using $K^{14}NO_3$ or $K^{15}NO_3$ for NO_3RR. (e) NH_3 Faradaic efficiency and (f) NH_3 partial current density and production rate of NiPr-TPA-COF in 0.5 M K_2SO_4 with the addition of different KNO_3 concentrations. (g) Cycling test of NiPr-TPA-COF at -1.38 V showing the average NH_3 Faradaic efficiency and production rate within each cycle.

spectrophotometry (Fig. S10, ESI†).[38] Its corresponding Faradaic efficiency was derived for different samples and plotted with respect to the working potential as shown in Fig. 2a. Worth noting is that both NiPr-TPA-COF and NiPr have remarkable NH_3 selectivity between -1.3 V and -1.5 V. In particular, the former exhibits a great value of >80% over the potential region examined, and delivers the maximum selectivity of ~90% at -1.38 V, superior to most single atom catalysts (SACs)[25, 39] and some Cu-based electrocatalysts previously reported under similar conditions.[40] The NH_3 Faradaic efficiency of NiPr starts to decline at <-1.4 V owing to the competition of HER. These two samples share the same NiPr moieties that are believed to be catalytically active sites. Metal-free H_2Pr-TPA-COF has much inferior selectivity of <30%, which clearly manifests the critical role of Ni^{2+} centers during NO_3RR.

The potential-dependent NH_3 partial current density and production rate were then calculated. They are observed to continuously rise with the increasing overpotential (Fig. 2b). At -1.46 V, the NH_3 partial current density of NiPr-TPA-COF reaches 31.2 mA cm^{-2}, and its NH_3 production rate reaches 2.5 mg cm^{-2} h^{-1}. These values are ~3 times larger than those of NiPr and >60 times larger than those of H_2Pr-TPA-COF. They are also orders of magnitude larger than the reported rates for electrochemical N_2 reduction to NH_3. Moreover, we estimated TOF by normalizing the NH_3 partial current density over the amount of surface accessible Ni sites (Fig. S11, ESI†). It is derived to be 12754 h^{-1} (or 3.5 s^{-1}) on NiPr-TPA-COF and 1717 h^{-1} (or 0.5 s^{-1}) on NiPr (Fig. 2c), reflecting a significantly higher site-specific activity when NiPr moieties are incorporated within the molecular frameworks. Among very few studies that actually reported TOFs for NO_3RR to NH_3, Ni nanoparticles were previously disclosed to have a TOF value of ~6 h^{-1} (or 0.0017 s^{-1}) at -0.5 V vs. RHE.[41] The orders-of-magnitude higher TOF value observed for our NiPr-TPA-COF highlights its extraordinary activity. To confirm the chemical origin of NH_3, ^{15}N-labeled isotope experiments were carried out on NiPr-TPA-COF (Fig. 2d). The ^1H NMR spectrum of normal $^{14}NH_3$ features a triplet with a coupling constant of 52 Hz. When $K^{15}NO_3$ is used instead of $K^{14}NO_3$, the ^1H NMR spectrum of its reduction product exhibits a distinct doublet with a coupling constant of 72 Hz that is characteristic of $^{15}NH_3$.[42] It supports that KNO_3 rather than other possible nitrogen contaminants is reduced during NO_3RR to yield NH_3 at high rates.

Our catalyst can work under a range of KNO_3 concentrations. Running the reaction in 0.05 M KNO_3 slightly compromises the NH_3 selectivity, and reduces the NH_3 production rate of NiPr-TPA-COF as expected. But even so, it still exhibits NH_3 selectivity of ~80% within -1.3~-1.4 V and a production rate of ~1.3 mg cm^{-2} h^{-1} at -1.46 V (Fig. 2e,f). The capability to work with low-concentration KNO_3 infers the great potential of our catalyst for converting wastewater nitrate (typically 0.01~0.1 M) into valuable NH_3. On the other hand, increasing the KNO_3 concentration to 0.3 M in the electrolyte boosts both the selectivity (close to unity) and activity (6.6 mg cm^{-2} h^{-1} at -1.42 V) of NiPr-TPA-COF. There is no sign of catalyst poisoning at high substrate concentrations, which is a concern for Cu-based materials.[13, 43, 44] Our NiPr-TPA-COF can also enable efficient NO_2RR to NH_3 in 0.5 M K_2SO_4 with 0.1 M KNO_2 (Fig. S13, ESI†). Its high NH_3 selectivity (~100% at -1.33 V) and great activity (5.3 mg cm^{-2} h^{-1} or 67 mA cm^{-2} at -1.44 V) also render it one of the best NO_2RR electrocatalysts in the neutral solution. Moreover, the effect of catalyst loading was explored and summarized in Fig. S12 (ESI†). Replacing the Ni centers with Co centers in CoPr-TPA-COF results in lower NH_3 selectivity and production rate (Fig. S14-15, ESI†). In addition to high activity and selectivity, operation stability is an important metric in the evaluation of catalysts. We find that when NiPr-TPA-COF is biased at a relatively negative working potential (*e.g.* -1.38 V), its cathodic current density is subjected to a rapid increase in the first 100-200 s and then gradually declines afterward (Fig. S16, ESI†). Such a dynamic evolution of current density reflects an activation-to-deactivation process that appears common to NO_3RR electrolysis.[43] The accumulation of side reduction products near the catalyst is believed to block its active sites for selective NO_3RR, which might explain the gradual but considerable deactivation.[45] Nevertheless, this deactivation causes no damage to the catalyst since its original activity could be fully recovered once the electrolyte is refreshed. We attempted to eliminate the deactivation process by using pulse electrolysis which has been demonstrated as an efficient tool for surface poison removal or catalyst regeneration.[46-51] The running program was set to consist of alternating reduction steps at -1.38 V for 1000 s and oxidation steps at +0.4 V for 1 s. During the cathodic step, NO_3RR takes place at the working electrode; during the anodic step, the side reduction products accumulated on the catalyst surface are quickly oxidized. In this way, our catalyst can be periodically regenerated without sacrificing current density or NH_3 selectivity. Its current density goes back to the initial level after the anodic step. As a result, long-term electrolysis could be carried out without interruption for ~20000 s (Fig. S17, ESI†). During the course of the measurement, the cathodic current density at the reduction steps stays ~20 mA cm^{-2}, and the average NH_3 Faradaic efficiency is ~73% (Fig. 2g). XRD, FT-IR and TEM characterizations of the catalyst after the long-term electrolysis reveal no discernible structural change at different scales, further attesting to its great stability (Fig. S18, ESI†).

In order to gain insights into the great performance of NiPr-TPA-COF, DFT calculations were carried out to reveal the distinct electronic structures in comparison with metal-free H_2Pr-TPA-COF (Fig. S19, ESI†). The projected partial density of state (PDOS)

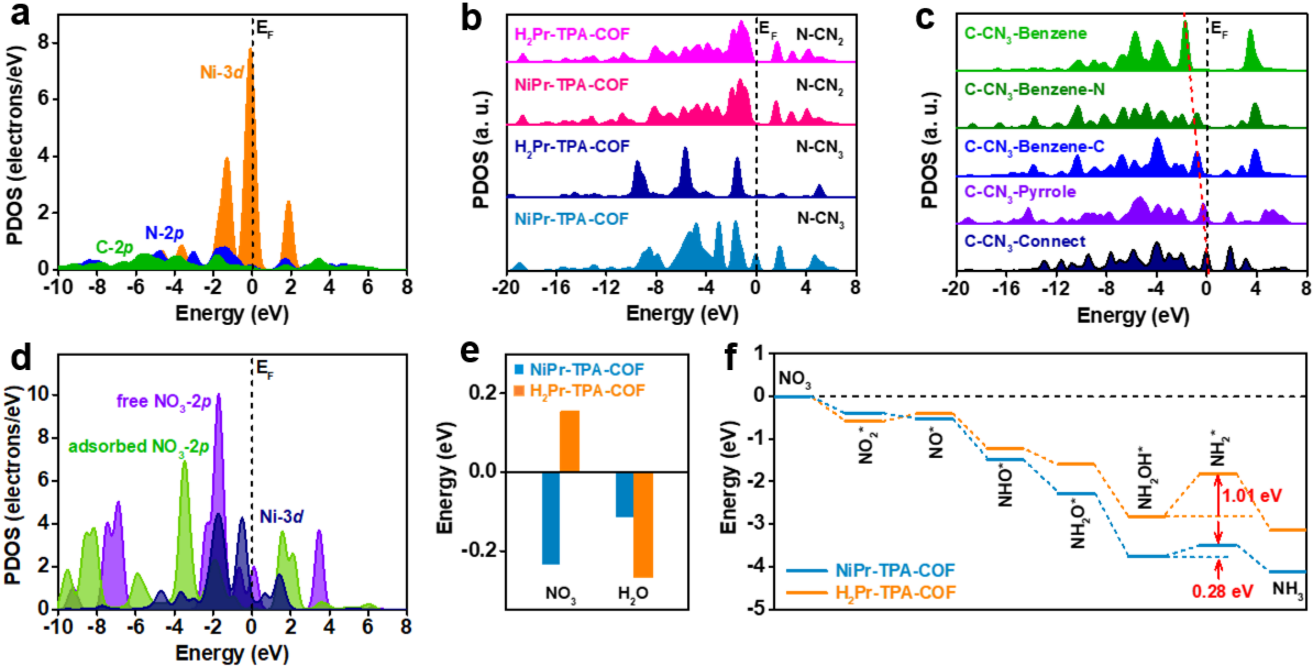

Fig. 3 DFT simulations of the catalyst electronic states and NO_3RR pathway. (a) PDOSs of NiPr-TPA-COF. (b) Site-dependent PDOSs of N-*2p* in NiPr-TPA-COF and H_2Pr-TPA-COF. (c) Site-dependent PDOSs of C-*2p* in NiPr-TPA-COF. (d) PDOSs of free NO_3 and NO_3 adsorbed on NiPr-TPA-COF. (e) Adsorption energies of NO_3 and H_2O on NiPr-TPA-COF and H_2Pr-TPA-COF. (f) Energetic reaction pathways of NO_3RR to NH_3 on NiPr-TPA-COF and H_2Pr-TPA-COF.

analysis shows that its Ni-*3d* orbitals are located close to the Fermi level (E_F), evidencing a high catalytic activity (Fig. 3a). They also exhibit a peak at E_v -1.30 eV (E_v denotes 0 eV) that considerably overlaps with both N-*2p* and C-*2p* orbitals, which may enable fast site-to-site electron transfer from surrounding C and N sites to the Ni center. When comparing the N-*2p* orbitals in NiPr-TPA-COF and H_2Pr-TPA-COF, it comes to our attention that the Ni center activates nearby N sites (N-CN_3) as reflected by their evidently increased electron density near the E_F (Fig. 3b). The N sites far away from the metal center and with a coordination number (CN) of two (N-CN_2) are not affected. Similarly, the Ni center also influences nearby C sites in the porphyrin, and increases their electron density near the E_F (Fig. 3c). Even at the benzene linker, carbon atoms adjacent to the imine group show upshifted C-*2p* orbitals relative to those connecting to H. These results reveal a gradual downshifting trend of C-*2p* orbitals in NiPr-TPA-COF that forms an efficient electron path for electrolysis. Moreover, the PDOS of NO_3 adsorption is analyzed in order to disclose the interaction between the catalyst and the reactant (Fig. 3d). The *2p* orbitals of free NO_3^- ions show a sharp peak at E_v -1.70 eV, which is close to the Ni-3d peaks. This can enable efficient electron transfer from NiPr-TPA-COF to NO_3^- with small energy barriers. Once NO_3^- ions are adsorbed, we observe that the strong interaction noticeably downshifts the *2p* orbitals of NO_3*, supporting the electron transfer from the Ni site. Accordingly, the Ni-*3d* orbitals are also modulated. The good orbital overlap between them ensures the stable adsorption of NO_3^* for further reduction. This also supports that the Ni center is the catalytic site for NO_3RR.

Further, we calculated the adsorption energies of NO_3 and H_2O on the two catalysts (Fig. 3e). Worth noting is that the adsorption of NO_3 on NiPr-TPA-COF (-0.23 eV) is spontaneous owing to its strong binding to the Ni center as explained above, while the adsorption of NO_3 on metal-free H_2Pr-TPA-COF (0.15 eV) is endothermic that may hinder its subsequent reduction. This confirms the enhanced binding strength of N-containing intermediates on Ni sites, which are significant to guarantee the stable fixation of intermediates for ammonia formation. The adsorption of H_2O is thermodynamically favorable on both NiPr-TPA-COF (-0.11 eV) and H_2Pr-TPA-COF (-0.27 eV), but its stronger binding on the latter may enhance the competing HER process and lower NO_3RR efficiency. The reduction mechanism of nitrate reduction is complicated, which involves 9 electron transfers in the process with valence state changes [52,53]. Fig. 3f depicts the simulated full reduction pathway from nitrate to ammonia [54]. Nitrate is first adsorbed on the catalyst surface, and dissociates to NO_2* and then NO*. Subsequently, NO* undergoes three proton-coupled electron transfers and is converted to NH_2OH* before further reduction to NH_3 and final desorption from the catalyst surface. We find that the reaction is overall downhill on NiPr-TPA-COF with an energy release of 4.1 eV.

Compared to H_2Pr-TPA-COF, it has stronger affinities towards

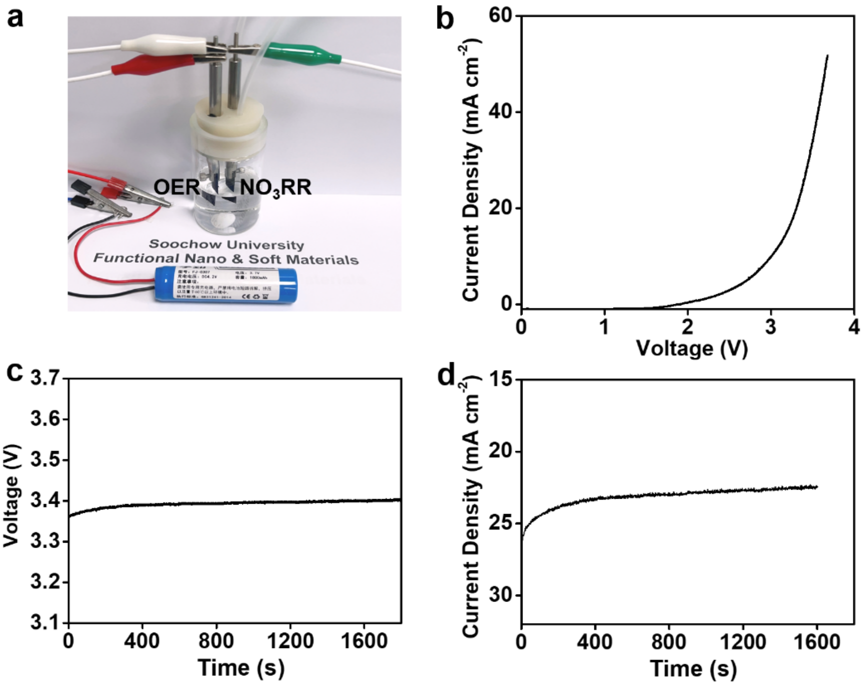

Fig. 4 Full-cell NO_3RR-OER electrolysis. (a) Photograph showing the setup for battery-powered NO_3RR-OER electrolysis. (b) Full-cell polarization curve. (c) Voltage change and (d) current evolution for the full-cell electrolysis.

all the intermediates except for NO_2^*. The reduction step from NH_2OH^* to NH_2^* is identified to be the rate-determining step for both catalysts, and its energy barrier is lowered from 1.01 eV on H_2Pr-TPA-COF to 0.28 eV on NiPr-TPA-COF. In addition to its favorable electronic structure, we believe that the highly ordered and porous structure of NiPr-TPA-COF may facilitate the mass transport, *i.e.* the diffuse-in of reactants (NO_3^- and H_2O) and the diffuse-out of products (NH_3 and OH^-). Its conjugated molecular frameworks may also form conductive pathways for efficient electron transfer to active centers. All these factors combined lead to the great NO_3RR activity and selectivity experimentally observed on NiPr-TPA-COF.

Having established NiPr-TPA-COF as a promising NO_3RR electrocatalyst, at last, we explored its potential in the coupled electrolysis of NO_3RR and oxygen evolution reaction (OER). A two-electrode configuration was assembled by pairing the NiPr-TPA-COF cathode with a piece of IrO_2-coated Ti mesh (IrO_2@Ti) as the anode (Fig. 4a). Fig. 4b presents the polarization curve without iR compensation. It starts to take off at 2.4 V and delivers 34 mA cm^{-2} at 3.5 V. A lithium-ion battery was then used to power the two-electrode cell. Under the voltage of ~3.4 V (Fig. 4c), the full reaction can be driven at a current density of 23 mA cm^{-2} (Fig. 4d). The average NH_3 Faradaic efficiency and energy efficiency are measured to be 91% and 14.5%, respectively. The experiment here demonstrates the practical viability of battery-driven NO_3RR using our catalyst. To further improve the energy efficiency, future optimization can be approached by carrying out the coupled reaction in the alkaline solution, replacing IrO_x/C with more active $NiFeO_x$ catalysts for OER, or substituting the sluggish anodic half-reaction with the electrochemical oxidation of alcohols (such as benzyl alcohol and glycerol).

Conclusions

In summary, we here reported the first demonstration of COF-based NO_3RR electrocatalysis to NH_3. NiPr-TPA-COF was prepared via the reversible Schiff base condensation reaction between amine-terminated NiPr and TPA. The product featured great structural crystallinity and abundant mesoporosity as characterized by a multitude of spectroscopic and microscopic techniques. When assessed as the electrocatalyst for NO_3RR in neutral solution, NiPr-TPA-COF exhibited near-unity NH_3 selectivity, great NH_3 production rate up to 2.5 mg h^{-1} $cm^{-2,}$ and TOF of 3.5 s^{-1} at -1.46 V. These values were superior to single atom catalysts and Cu-based materials under similar conditions. Moreover, it had great stability that could be periodically recovered and was further improved under pulse electrolysis. DFT simulations revealed that NiPr-TPA-COF had unique electronic structures that enhanced its interaction with NO_3, and facilitated electron transfer during electrocatalysis. The presence of the Ni center considerably lowered the activation energy barrier of the rate-determining step. At last, we demonstrated the coupled electrolysis of NO_3RR and OER by combining NiPr-TPA-COF as the cathode catalyst and IrO_2@Ti as the anode catalyst. When powered by a lithium-ion battery, the two-electrode cell stably delivered a current density of 23 mA cm^{-2} and great NH_3 selectivity of 91%. Our study here showcases the great potential of transition metal macrocycles for selective NO_3RR to NH_3. The catalyst reported here is consisted of earth-abundant elements (C, H, and N) and a small fraction of Ni, and is potentially more cost-effective than other candidate catalysts.

Author Contributions

Y. Li proposed the concept and designed all experimental studies. Y. Hu, W. Huang, and F. Lv carried out materials synthesis, characterization, and electrochemical NO_3RR measurements. J. Xu. performed the TEM analysis. B. Huang and M. Sun designed and performed DFT calculations. All authors contribute to the preparation of the manuscript.

Conflicts of interest

There are no conflicts to declare.

Acknowledgements

We acknowledge the support from the National Natural Science Foundation of China (U2002213, 52161160331 and 21902114), the Science and Technology Development Fund Macau SAR (0077/2021/A2), the Collaborative Innovation Center of Suzhou Nano Science and Technology, the 111 Project, Joint International Research Laboratory of Carbon-Based Functional Materials and Devices, the NSFC/RGC Joint Research Scheme Project (N_PolyU502/21), and the funding for Projects of Strategic Importance of The Hong Kong Polytechnic University (Project Code: 1-ZE2V).

References

1 N. Gruber, J. N. Galloway, *Nature*, 2008, **451**, 293-296.
2 J. N. Galloway, A. R. Townsend, J. W. Erisman, M. Bekunda, Z. Cai, J. R. Freney, L. A. Martinelli, S. P. Seitzinger, M. A. Sutton, *Science*, 2008, **320**, 889-892.
3 H. Liu, Chin. *J. Catal.*, 2014, **35**, 1619-1640.
4 B. H. R. Suryanto, H. L. Du, D. Wang, J. Chen, A. N. Simonov, D. R. MacFarlane, *Nat. Catal.*, 2019, **2**, 290-296.

5 J. Choi, B. H. Suryanto, D. Wang, H. L. Du, R. Y. Hodgetts, F. M. Ferrero Vallana, D. R. MacFarlane, A. N. Simonov, *Nat. Commun.*, 2020, **11**, 5546.

6 G. Soloveichik, *Nat. Catal.*, 2019, **2**, 377-380.

7 F. Lv, S. Zhao, R. Guo, J. He, X. Peng, H. Bao, J. Fu, L. Han, G. Qi, J. Luo, X. Tang, X. Liu, *Nano Energy*, 2019, **61**, 420-427.

8 P. H. van Langevelde, I. Katsounaros, M. T. M. Koper, *Joule*, 2021, **5**, 290-294.

9 Y. Wang, C. Wang, M. Li, Y. Yu, B. Zhang, *Chem. Soc. Rev.*, 2021, **50**, 6720-6733.

10 Y. Zeng, C. Priest, G. Wang, G. Wu, *Small Methods*, 2020, **4**, 2000672.

11 Y. Ren, C. Yu, L. Wang, X. Tan, Z. Wang, Q. Wei, Y. Zhang, J. Qiu, *J. Am. Chem. Soc.*, 2022, **144**, 10193-10200.

12 J. Sun, D. Alam, R. Daiyan, H. Masood, T. Zhang, R. Zhou, P. J. Cullen, E. C. Lovell, A. R. Jalili, R. Amal, *Energy Environ. Sci.*, 2021, **14**, 865-872.

13 S. Garcia-Segura, M. Lanzarini-Lopes, K. Hristovski, P. Westerhoff, *Appl. Catal. B*, 2018, **236**, 546-568.

14 A. Bhatnagar, M. Sillanpää, *Chem. Eng. J.*, 2011, **168**, 493-504.

15 F. Y. Chen, Z. Y. Wu, S. Gupta, D. J. Rivera, S. V. Lambeets, S. Pecaut, J. Y. T. Kim, P. Zhu, Y. Z. Finfrock, D. M. Meira, G. King, G. Gao, W. Xu, D. A. Cullen, H. Zhou, Y. Han, D. E. Perea, C. L. Muhich, H. Wang, *Nat. Nanotechnol.*, 2022, **17**, 759-767.

16 V. Rosca, M. Duca, M. T. de Groot, M. T. M. Koper, *Chem. Rev.*, 2009, **109**, 2209-2244.

17 Y. Wang, A. Xu, Z. Wang, L. Huang, J. Li, F. Li, J. Wicks, M. Luo, D. H. Nam, C. S. Tan, Y. Ding, J. Wu, Y. Lum, C. T. Dinh, D. Sinton, G. Zheng, E. H. Sargent, *J. Am. Chem. Soc.*, 2020, **142**, 5702-5708.

18 Y. Wang, W. Zhou, R. Jia, Y. Yu, B. Zhang, *Angew. Chem. Int. Ed.*, 2020, **59**, 5350-5354.

19 G. F. Chen, Y. Yuan, H. Jiang, S. Y. Ren, L. X. Ding, L. Ma, T. Wu, J. Lu, H. Wang, *Nat. Energy*, 2020, **5**, 605-613.

20 W. Jung, Y. J. Hwang, Mater. Chem. Front., 2021, 5, 6803-6823.

21 S. Yang, Y. Yu, X. Gao, Z. Zhang, F. Wang, *Chem. Soc. Rev.*, 2021, **50**, 12985-13011.

22 S. Dey, B. Mondal, S. Chatterjee, A. Rana, S. Amanullah, A. Dey, *Nat. Rev. Chem.*, 2017, **1**, 0098.

23 F. Lv, N. Han, Y. Qiu, X. Liu, J. Luo, Y. Li, *Coord. Chem. Rev.*, 2020, **422**, 213435.

24 N. Han, Y. Wang, L. Ma, J. Wen, J. Li, H. Zheng, K. Nie, X. Wang, F. Zhao, Y. Li, J. Fan, J. Zhong, T. Wu, D. J. Miller, J. Lu, S. T. Lee, Y. Li, *Chem*, 2017, **3**, 652-664.

25 Z.-Y. Wu, M. Karamad, X. Yong, Q. Huang, D. A. Cullen, P. Zhu, C. Xia, Q. Xiao, M. Shakouri, F. Y. Chen, J. Y. T. Kim, Y. Xia, K. Heck, Y. Hu, M. S. Wong, Q. Li, I. Gates, S. Siahrostami, H. Wang, *Nat. Commun.*, 2021, **12**, 2870.

26 L. Sun, V. Reddu, A. C. Fisher, X. Wang, *Energy Environ. Sci.*, 2020, **13**, 374-403.

27 J. L. Segura, M. J. Mancheño, F. Zamora, *Chem. Soc. Rev.*, 2016, **45**, 5635-5671.

28 L. Cusin, H. Peng, A. Ciesielski, P. Samorì, *Angew. Chem. Int. Ed.*, 2021, **133**, 14356-14370.

29 W. Huang, W. Luo, Y. Li, *Mater. Today*, 2020, **40**, 160-172.

30 H. L. Nguyen, C. Gropp, O. M. Yaghi, *J. Am. Chem. Soc.*, 2020, **142**, 2771-2776.

31 Y. Li, L. Guo, Y. Lv, Z. Zhao, Y. Ma, W. Chen, G. Xing, D. Jiang, L. Chen, *Angew. Chem. Int. Ed.*, 2021, **133**, 5423-5429.

32 W. Dai, F. Shao, J. Szczerbiński, R. McCaffrey, R. Zenobi, Y. Jin, A. D. Schlüter, W. Zhang, *Angew. Chem. Int. Ed.*, 2016, **128**, 221-225.

33 S. Lin, C. S. Diercks, Y. B. Zhang, N. Kornienko, E. M. Nichols, Y. Zhao, A. R. Paris, D. Kim, P. Yang, O. M. Yaghi, *Science*, 2015, **349**, 1208-1213.

34 L. Sun, M. Lu, Z. Yang, Z. Yu, X. Su, Y. Q. Lan, L. Chen, *Angew. Chem. Int. Ed.*, 2022, **134**, e202204326.

35 X. Deng, Y. Yang, L. Wang, X. Z. Fu, J. L. Luo, *Adv. Sci.*, 2021, **8**, 2004523.

36 J. Li, G. Zhan, J. Yang, F. Quan, C. Mao, Y. Liu, B. Wang, F. Lei, L. Li, A. W. M. Chan, L. Xu, Y. Shi, Y. Du, W. Hao, P. K. Wong, D. Wang, J. Shi-Xue, L. Zhang, J. C. Yu, *J. Am. Chem. Soc.*, 2020, **142**, 7036-7046.

37 J. Yang, H. Qi, A. Li, X. Liu, X. Yang, S. Zhang, Q. Zhao, Q. Jiang, Y. Su, L. Zhang, J. Li, Z. Tian, W. Liu, A. Wang, T. Zhang, *J. Am. Chem. Soc.,* 2022, **144,** 12062-12071.

38 P. L. Searle, *Analyst*, 1984, **109**, 549-568.

39 W. D. Zhang, H. Dong, L. Zhou, H. Xu, H. R. Wang, X. Yan, Y. Jiang, J. Zhang, Z.-G.L. Gu, *Appl. Catal., B,* 2022, **317**, 121750.

40 J. Wang, T. Feng, J. Chen, V. Ramalingam, Z. Li, D. M. Kabtamu, J. H. He, X. Fang, *Nano Energy*, 2021, **86**, 106088.

41 P. Gao, Z. H. Xue, S. N. Zhang, D. Xu, G. Y. Zhai, Q. Y. Li, J. S. Chen, X. H. Li, *Angew. Chem. Int. Ed.*, 2021, **133**, 20879-20884.

42 A. C. Nielander, J. M. McEnaney, J. A. Schwalbe, J. G. Baker, S. J. Blair, L. Wang, J. G. Pelton, S. Z. Andersen, K. Enemark-Rasmussen, V. Čolić, S. Yang, S. F. Bent, M. Cargnello, J. Kibsgaard, P. C. K. Vesborg, I. Chorkendorff, T. F. Jaramillo, *ACS Catal.*, 2019, **9**, 5797-5802.

43 K. S. Rajmohan, R. Chetty, *ECS Trans.*, 2014, **59**, 397-407.

44 H. Xu, Y. Ma, J. Chen, W. X. Zhang, J. Yang, *Chem. Soc. Rev.*, 2022, **51**, 2710-2758.

45 D. Reyter, D. Bélanger, L. Roué, *Electrochim. Acta*, 2008, **53**, 5977-5984.

46 C. W. Lee, N. H. Cho, K. T. Nam, Y. J. Hwang, B. K. Min, *Nat. Commun.,* 2019, **10,** 3919.

47 R. Casebolt, K. Levine, J. Suntivich, T. Hanrath, *Joule,* 2021, **5**, 1987-2026.

48 H. S. Jeon, J. Timoshenko, C. Rettenmaier, A. Herzog, A. Yoon, S. W. Chee, S. Oener, U. Hejral, F. T. Haase, B. Roldan Cuenya, *J. Am. Chem. Soc.,* 2021, **143,** 7578-7587.

49 L. Gao, L. Ding, L. Fan, *Electrochim. Acta,* 2013, **106,** 159-164.

50 T. Liu, J. Wang, X. Yang, M. Gong, *J. Energy Chem.,* 2021, **59,** 69-82.

51 C. Kim, L. C. Weng, A. T. Bell, *ACS Catal.,* 2020, **10,** 12403-12413.

52 Y. Wang, C. Wang, M. Li, Y. Yu, B. Zhang, *Chem. Soc. Rev.*, 2021, **50**, 6720-6733

53 M. Duca, M. T. M. Koper, *Energy Environ. Sci.*, 2012, **5**, 9726-9742.

54 P. Li, Z. Jin, Z. Fang, G. Yu, *Energy Environ. Sci.*, 2021, **14**, 3522-3531.